



Silver-photodeposited TiO₂-clay nanocomposite: sol–gel synthesis, characterization and CCD-optimized photocatalytic activity

Abdelali El Gaidoumi^{1,2} · Karim Tanji² · Amal Loqman² · Imane El Mrabet³ · Youssef Fahoul² · Abdellah Arrahli^{2,4} · Abdelaziz Dra² · Morad Zouheir² · Brahim El Bali⁵ · Abdelhak Kherbeche²

Received: 18 May 2022 / Accepted: 30 August 2022 / Published online: 24 September 2022
© Iranian Chemical Society 2022

Abstract

Nanocomposites of TiO₂-clay were synthesized by the sol–gel route. The materials were characterized by XPS, XRD, UV–Vis DRS and BET surface area. Photocatalytic activity under UV irradiation ($\lambda_{\max} \approx 365$ nm) was investigated by means of the phenol oxidation reaction. It was observed that the UV-photocatalytic property of TiO₂-clay nanocomposite (SG) ($E_{\text{gap}} = 3.17$ eV, $S_{\text{BET}} = 16.58$ m² g⁻¹) for the phenol photodegradation was higher than that of commercial AEROXIDE® TiO₂ P25. The activity of SG was greatly improved after silver photodeposition; in fact, the silver-photodeposited into SG highly enhanced the phenol degradation and mineralization efficiencies. The optimization of different experimental parameters, such as the photocatalyst amount, pH, temperature or hydrogen peroxide concentration on the phenol photodegradation under UV irradiation was studied with photodeposited catalyst 1.5%Ag/SG ($E_{\text{gap}} = 3.12$ eV, $S_{\text{BET}} = 12.16$ m² g⁻¹) based on the response surface methodology selecting composite central design as statistical model. Based on the ANOVA analysis, simulations explained a good fit to the experimental data involving a second-degree polynomial model with a model *F*-value of 73.31 and coefficient of determination (R^2) value of 0.9959. Optimal experimental conditions were found to be a photocatalyst amount of 2 g L⁻¹, solution pH of 5, temperature of 40 °C and hydrogen peroxide concentration of 8 mmol L⁻¹. Under these optimized conditions, total degradation, 91% mineralization and non-toxicity were found, at 50 mg L⁻¹ phenol during 120 min of reaction. Overall, pyrophyllite clay is very attractive as a natural and low-cost mineral for elaborating efficient photocatalysts.

Keywords Pyrophyllite · Sol–gel · Photocatalysis · Phenol · Photodeposition · TiO₂

Introduction

As a result of traditional disposal practices of agricultural, industrial and sewage wastes, there has been an increase in the toxicity of water bodies which affects both human and wild health. Most industrial wastes containing toxic compounds are discharged into natural water bodies without adequate treatment [1–7]. Phenol-based compounds are the chemical residues of byproducts/wastes of several industries such as petroleum refineries, paper mills, pharmaceuticals, pesticides, coke plants, polymeric resin, coal conversion and paint [8, 9]. Therefore, numerous studies have been investigated for the treatment of phenolic wastes before their release in the nature [10, 11]. The literature reports on three techniques for the elimination of phenols from waters: biological, physical and chemical. The most widely applicable techniques are coagulation, precipitation, ion exchange, filtration, adsorption, solvent extraction and

✉ Karim Tanji
karim.tanji@usmba.ac.ma

¹ Laboratoire de Biotechnologie, Bioressources et Bioinformatique (3Bio), École Supérieure de Technologie de Khénifra, Université Sultan Moulay Slimane, Béni Mellal, Morocco

² Laboratoire de Matériaux, Procédés, Catalyse et Environnement (LMPCE), École Supérieure de Technologie de Fès, Université Sidi Mohamed Ben Abdellah, Fès, Morocco

³ Department of Physics–Chemistry, Polydisciplinary Faculty of Ouarzazate, University of Ibn Zohr, Ouarzazate, Morocco

⁴ Centre de Recherche Euromed, Institut International des Sciences Appliquées Euro-Méditerranée, Université Euro-Méditerranéenne de Fès (UEMF), Fès, Morocco

⁵ Oujda, Morocco

advanced oxidation processes (AOPs) [12–16]. Several studies have been extensively highlighted the use of the photocatalysis process, one of the AOPs, in hydrogen production and water purification [17–19]. It is especially adequate for the depollution of low liquid volumes containing low pollutants concentrations. This technique is based on the efficiency of a semiconductor, which could be photo-illuminated with energy greater than its band-gap producing electron–hole ($e^- - h^+$) pairs. These latest can emigrate to the semiconductor surface generating radicals that can initiate redox reactions [20]. The effectiveness of these reactions is related to the advantage of the high reactive radicals HO in driving oxidation processes, which are convenient for performing complete degradation and mineralization of even most less and persistent reactive compounds.

The synthesis of porous photocatalysts assembled, or immobilized by nanostructured semiconductors, might be a tricky manner to design porous materials with higher photoactivity properties. This could be the case when fixing a semiconductor onto solids such as zeolites, diatomite, activated carbon, kenyaite or clays [17, 21–24]. Clay minerals are promising photocatalyst supports because of their good adsorption capacity, their high mechanical and chemical stability, which reduces the aggregation of photocatalyst nanoparticles, leading to increased photocatalytic efficiency. Numerous layered clay-based catalysts have been extensively investigated such as modified organoclays, acid-modified clays, semiconductor-clay heterojunctions, pillared clays and delaminated clay heterostructures, characterized by higher quality porous morphologies [25–27].

The noble metals (e.g., Au, Pt, Pd, Ag, Cu) have received much interest for various applications in biotechnology, catalysis and environment [28–31]. It was previously reported the uses of such metals as photodeposition tools, more precisely the photodegradation of dyes, acids, phenol [32–35] and NO [36], and the H_2 production [37–39]. Among noble metals selected as electron traps, silver turned out to be highly beneficial for industrial applications, due to its low cost and easy preparation [40]. Silver-deposits on TiO_2 have been shown to mineralize mono-, di- and polycarboxylic acids [41] and remove the 2-propanol [42], and urea and chloroform [43]. Simultaneously, the nano size of silver particles, loading amount, preparation method, nature, pH and pollutant concentration influence the photocatalytic performance of silver-semiconductor nanomaterials [44]. Heretofore, silver- TiO_2 nanocomposites have been prepared by various chemical and physical techniques, like magnetron sputtering, electron beam evaporation, molecular precursor, sol–gel and photo-deposition [45–47].

Pyrophyllite, an aluminum silicate hydroxide [$Al_2(OH)_2Si_4O_{10}$], is a layered clay with crystal structure (Fig. 1) consists of an octahedral Al–O sheet sandwiched between two tetrahedral Si–O sheets, with each octahedral

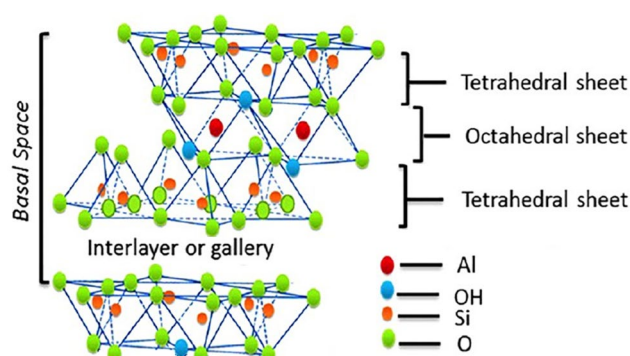


Fig. 1 Structure of pyrophyllite

aluminum bonded with tetrahedral silicon by apical oxygen and with adjacent aluminum by two hydroxyl groups [48]. Pyrophyllite has been widely used in many industries, including refractory bricks, plastics, papers, and ceramics [49]. In addition, several studies have been conducted on use this clay as an adsorbent for various pollutants in aqueous medium [50–53].

As to continue the research in the field of the pyrophyllite-nanocomposites, we report in the present paper on the sol–gel synthesis of the TiO_2 such nanocomposites and their photocatalytic performance. The prepared photocatalysts (SG and 1.5%Ag/SG) were tested in the photodegradation of phenol under UV irradiation. Moreover, the optimization of parameters (catalyst amount, pH, temperature, and H_2O_2 concentration) by response surface methodology in the phenol degradation with 1.5%Ag/SG was also studied.

Experimental

Materials

The local clay used in this paper has previously been investigated [54–61]. It is gray type clay and mainly composed of pyrophyllite-2M [$Al_2(Si_4O_{10})(OH)_2$], with weight composition: SiO_2 58%_{w/t}, Al_2O_3 26%_{w/t}, Fe_2O_3 2.7%_{w/t}, K_2O 1.6%_{w/t}, Na_2O 1.5%_{w/t}, MgO 0.8%_{w/t}, TiO_2 0.6%_{w/t} and CaO 0.12%_{w/t}. It was used in the present work after acid decarbonation as follows [62]: (1) solution made up of 100 mL hydrochloric acid (0.5 M) and 2 g of raw clay was aged for 1 h at room temperature. (2) After several washes, the resultant material was dried at 110 °C for 24 h and sieved with a 63 μm mesh (we refer to it below as PT). All chemicals that have been used in this present work are Sigma-Aldrich products: Titania powder (AEROXIDE® TiO_2 P25), titanium (IV) *t*-butoxide 97%_{w/t}, phenol 99.5%_{w/t}, ethanol 99.5%_{w/t}, sodium hydroxide 98%_{w/t}, hydrochloric acid 37%_{w/t}, muconic acid 97%_{w/t}, formic acid 98–100%_{w/t}, maleic acid 99%_{w/t}, hydrogen

peroxide 30%_{w/w}, and acetonitrile 99.8%_{w/w}. Milli-Q water was used in all the processes.

Preparation of the photocatalysts

SG nanocomposite material was synthesized via sol–gel technique as follows: (1) solution made up of 40 mL ethanol and 17 mL titanium (IV) *t*-butoxide $\text{Ti}(\text{OCH}_2\text{CH}_2\text{CH}_2\text{CH}_3)_4$ was dropwise added to another solution of 20 mL ethanol in which 2 g decarbonated clay was dispersed. (2) 30 mL ethanol diluted with 20 mL Milli-Q water was dropwise added until the formation of a dense gel. (3) The resultant gel was aged for 24 h. (4) After washing cycles, the gel was dried at 100 °C for 24 h. (5) The dried gel was sieved (63 μm) and then calcined at 750 °C for 4 h.

Silver was deposited into SG by photo-irradiation using a mercury UV lamp (400 W), isopropanol as a sacrificial reagent and silver nitrate as a source of Ag^+ ions. Photodeposition of 1.5%_{w/w} of Ag during 6 h was carried out in an anoxic medium achieved with a constant N_2 flow. This photocatalyst is referred to hereinafter as 1.5%Ag/SG.

Characterization and analytical techniques

X-ray diffraction (XRD) patterns were recorded on a diffractometer (Siemens D-500, $\lambda_{\text{Cu K}\alpha} = 1.5418 \text{ \AA}$) in the region of 5–80°. The morphology of the materials was performed by scanning electron microscopy (SEM) using a JEOL JSM-5400 microscope coupled with energy-dispersive x-ray spectroscopy (EDX). BET specific surface area was measured by N_2 adsorption at –196 °C using a Micromeritics ASAP 2010 system. X-ray photoelectron spectroscopy (XPS) characterization was conducted on a spectrometer (Leybold-Heraeus LHS-10). UV–Vis diffuse-reflectance spectrophotometry (UV–Vis DRS) analysis was performed in the range of 250–800 nm through a spectrophotometer (Varian Cary 5 UV-NIR) using polytetrafluoroethylene as reference. Concentrations of phenol and intermediate products were measured by high-performance liquid chromatography (HPLC) by means of a C18 column (0.25 m × 0.046 m ID, 5×10^{-6} m particles), detector (UV, $\lambda = 270 \text{ nm}$) and water-acetonitrile (70:30) as mobile phase. The determination of total organic carbon (TOC) was performed using Shimadzu TOC-VSCN analyzer. The toxicity of treated solutions was investigated by the Microtox toxicity test (standard ISO 11348-2:2007) as the inhibition of bioluminescence of *Vibrio fischeri* marine-bacteria. The inhibition below 10% indicates a solution is nontoxic.

Photocatalysis experiments of phenol

The experiments were performed in a 500 mL Pyrex cylindrical reactor. 200 mL phenol solution at 50 mg L^{-1} and

study amounts of photocatalyst were stirred and continuously bubbled by air (air flow = 400 mL min^{-1}). The reactor was irradiated from the outside using a UV lamp (Philips Solarium HB175) equipped with four fluorescent tubes (15 W, 365 nm).

Analysis of response surface modeling

Central composite design (CCD) was postulated to specify the operating conditions for optimizing the phenol degradation yield. The interaction between dependent and independent variables was studied following the second-degree polynomial:

$$Y = \alpha_0 + \alpha_1 X_1 + \alpha_2 X_2 + \alpha_3 X_3 + \alpha_4 X_4 + \alpha_{12} X_1 X_2 + \alpha_{13} X_1 X_3 + \alpha_{14} X_1 X_4 + \alpha_{23} X_2 X_3 + \alpha_{24} X_2 X_4 + \alpha_{34} X_3 X_4 + \alpha_{11} X_1^2 + \alpha_{22} X_2^2 + \alpha_{33} X_3^2 + \alpha_{44} X_4^2 \quad (1)$$

where X_i denotes the independent variables (catalyst amount, pH, temperature and H_2O_2 concentration), Y is the predicted response (phenol degradation yield), α_i is the linear effect, α_{ij} is the interaction effect, α_{ii} is the quadratic effect and α_0 is a constant offset term.

The Design Expert Software Version 11.0 (State-Ease, Minneapolis, USA) was used to analyze the experimental results [63].

Results and discussions

Characterizations

Figure 2 presents the diffractograms of the clay PT and photocatalysts. The PT sample exhibited (Fig. 2a) characteristic peaks of pyrophyllite phase $\text{Al}_2(\text{Si}_4\text{O}_{10})(\text{OH})_2$ at $2\theta = 9.62, 12.37, 20.85, 21.29, 26.63, 29.11, 34.96, 47.99, 56.43, 59.95, 62.37, 68.48$ (Ref. code: 00-046-1308) and characteristic peaks of quartz impurities at $2\theta = 26.63, 36.53, 39.46, 42.44, 45.79, 50.13$ (Ref. code: 01-089-8934), in good agreement with the literature [64–66]. The diffractogram of photocatalysts (Fig. 2b) shows anatase TiO_2 peaks at $2\theta = 68.8^\circ, 63.2^\circ, 62.7^\circ, 55.1^\circ, 53.9^\circ, 48.1^\circ, 37.9^\circ$ and 25.3° (JCPDS No. 21-1272) [67–78], rutile TiO_2 peaks at $2\theta = 56.6^\circ, 54.3^\circ, 36.1^\circ$ and 27.4° (JCPDS No. 75-1753) [72] and characteristic clay's peaks; but otherwise, no crystalline phases that might result from silver was observed in the 1.5%Ag/SG catalyst, which might be assigned to the low-doped silver [40, 74].

Table 1 summarizes the surface area and the ratio distribution of the TiO_2 Anatase–rutile forms in terms of particle size and composition for the photocatalysts. The results show that PT and SG have a surface area of $9.14 \text{ m}^2 \text{ g}^{-1}$ and

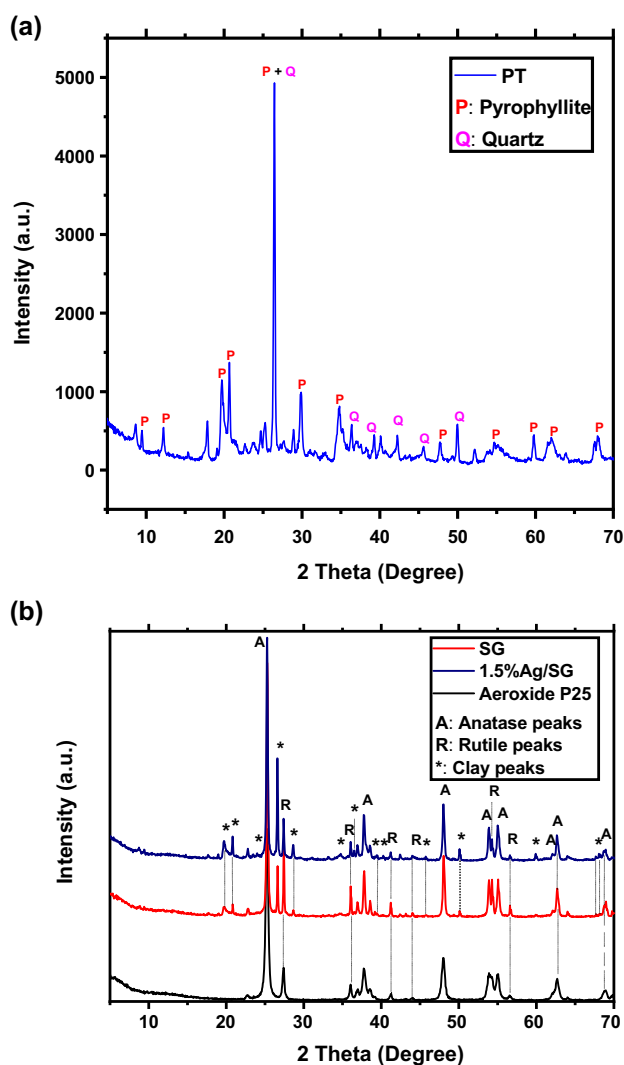


Fig. 2 XRD diffractograms of PT (a) and investigated photocatalysts (b)

$16.6 \text{ m}^2 \text{ g}^{-1}$, respectively. This increase in the surface area indicates the successful pillaring of the TiO_2 nanoparticles into the PT layers. In fact, the synthesis of SG was carried out in an aqueous medium containing titanium (IV) *t*-butoxide and PT, so the Ti ions were transformed into $\text{Ti}(\text{OH})_4$ intermediate. After the calcination step at $750 \text{ }^\circ\text{C}$, the

$\text{Ti}(\text{OH})_4$ was transformed into TiO_2 . Based on this transformation, we assumed that the ion exchange process was first initiated in the PT interlayers and, therefore, that TiO_2 pillaring is possible within the layered PT. Indeed, the exchangeable cations in the PT interlayers were substituted by Ti^{4+} ions which were hydrolyzed to $\text{Ti}(\text{OH})_4$ and then converted to TiO_2 after calcinations [79]. In addition, photodeposition negatively affected the surface area and crystal size of SG, probably due to the additional incorporation of Ag particles into the SG pores. The synthesis of SG and 1.5%Ag/SG implies the generation of mesopores as a significant issue, which can be confirmed by the important participation of mesoporosity to the external surface area attributing non-microporous part (Table 1).

The mesopores are essentially distributed within the diameter range of 3.5–4.5 nm (Fig. 3a). The porous structure of the SG and 1.5%Ag/SG, which is due to the clay layers [75], was also proven by the N_2 adsorption–desorption isotherms represented in Fig. 3b. Both photocatalysts showed a type II isotherm according to the IUPAC classification with a H3 hysteresis loop [76, 77]. This type of isotherm has been discussed in several investigations, described by porous materials due to a house-of-cards structure produced by the plate-like aggregates [69, 78].

To confirm that the TiO_2 crystals and Ag particles were well dispersed in the photocatalysts, SEM analysis (Fig. 4) was performed. The SEM image of PT (Fig. 4a) shows that it is layered clay, while the SEM image of SG (Fig. 4b) insures that TiO_2 crystals were incorporated into the clay layers. Figure 4c illustrates the Ag and Ti SEM mapping images and semiquantitative EDX analysis of 1.5%Ag/SG. It can be seen that Ti and Ag were homogeneously dispersed along the surface. Moreover, The EDX shows good photodeposition of Ag metal on SG as confirmed by its weight percentage very near 1.5%.

The XPS analysis was performed for 1.5%Ag/SG in order to specify the oxidation state of Ti, Ag and O (Fig. 5). The Ag 3d XPS spectrum (Fig. 5b) of 1.5%Ag/SG shows two peaks at 373.8 eV and 367.8 eV attributed to the Ag $3d_{3/2}$ and $3d_{5/2}$ core levels, respectively [44, 70, 80]. The gap energy separation between Ag $3d_{3/2}$ and $3d_{5/2}$ is equal to 6.0 eV demonstrating the presence of silver in the chemical state of Ag° [81]. The absence of Ag^+ ions indicates their reduction to Ag

Table 1 Anatase–rutile ratio, crystalline size, surface area, and band gap of photocatalysts

Samples	Anatase (A)/Rutile (R) ratio	Crystalline size (nm)		Surface area ($\text{m}^2 \text{ g}^{-1}$)		Band gap (eV)
		Anatase	Rutile	S_{BET}	S_{EXT}	
PT	–	–	–	9.14	7.35	2.89
P25	80% A/20% R	22.1	24.8	52	51.2	3.19
SG	52.2% A/10.7% R	35.5	60.8	16.6	15.7	3.17
1.5%Ag/SG	49.6%A/12.4% R	19.4	61.7	12.7	8.1	3.12

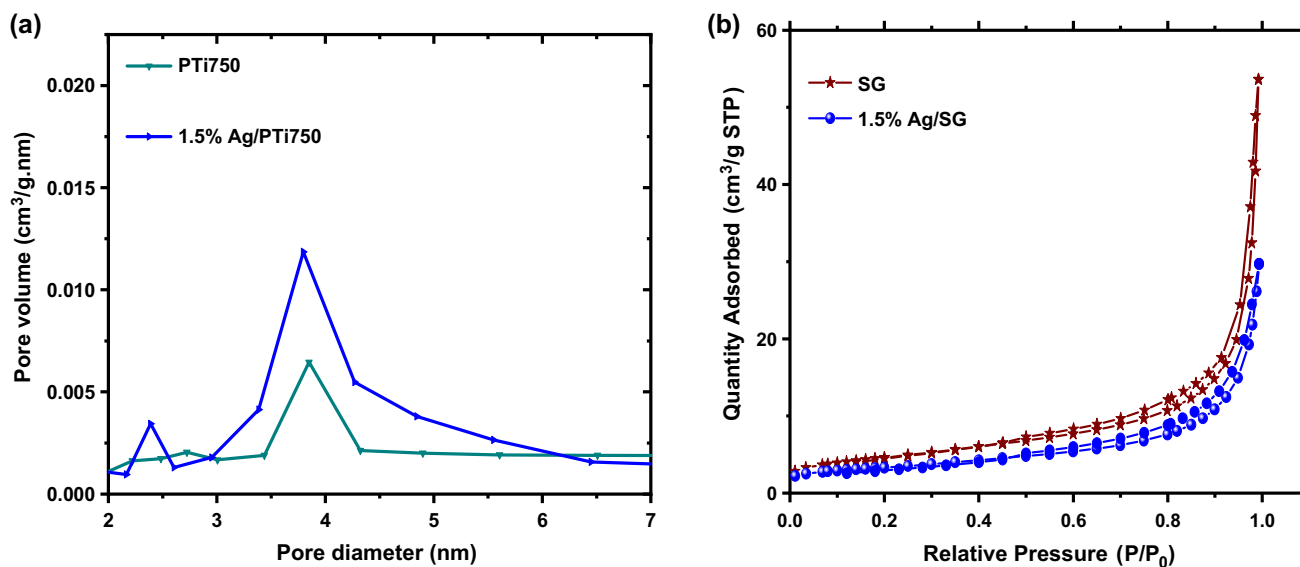
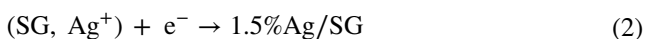


Fig. 3 Pore size distribution (a) and N_2 adsorption–desorption isotherms of prepared photocatalysts (b)

(Eq. 2) [70, 80, 81]. The peaks of Ag 3d shift negatively compared to bulk Ag^0 ones (374 or 374.3 eV for $Ag\ 3d_{3/2}$ and 368 or 368.3 eV for $Ag\ 3d_{5/2}$), indicating that the electrons may migrate from TiO_2 to Ag, which confirms that there is a strong TiO_2 –Ag interaction in the interface of the photocatalyst [82, 83]. As shown in Fig. 5c, the Ti 2p XPS spectra of 1.5%Ag/SG with two peaks at binding energies of 458.0 eV and 463.8 eV, correspond to the Ti $2p_{3/2}$ and Ti $2p_{1/2}$ orbits, respectively [69]. The gap of 5.8 eV between these orbits confirms the existence of the Ti^{4+} oxidation state reported in TiO_2 [44, 74, 84]. From Fig. 5d, the O 1s XPS spectra of 1.5%Ag/SG show a peak located at 529.7 eV which is ascribed to lattice oxygen (Ti–O bond) comes from TiO_2 [84].



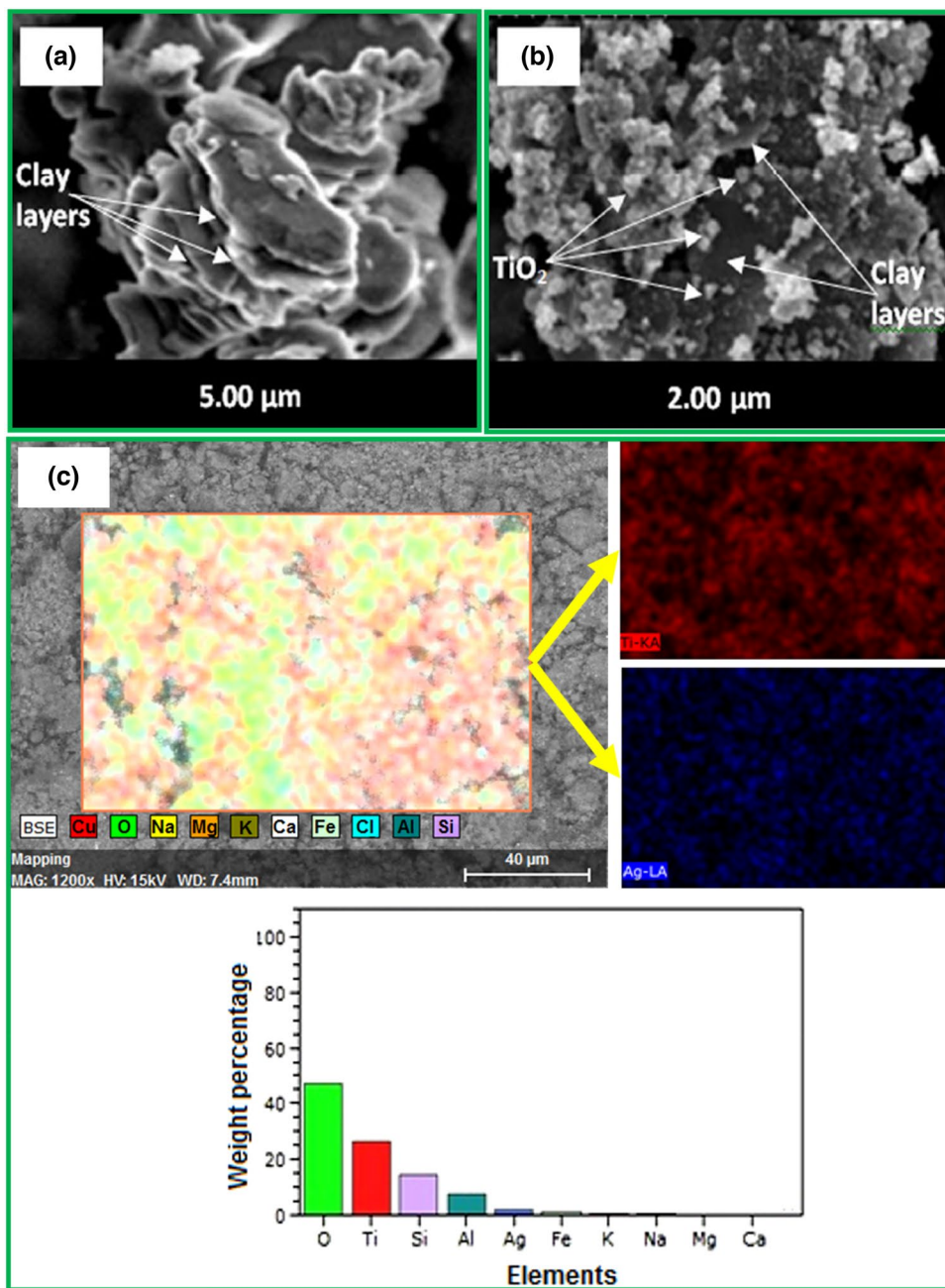
UV–Vis DRS analysis of the photocatalysts (Fig. 6, Table 1) was performed and their band gap values were determined using Tauc’s plot following this formula $(\alpha h\nu)^2 = A(h\nu - E_g)$ [15]. The difference observed between band gap energies of SG (3.17 eV) and 1.5%Ag/SG (3.12 eV) is not relevant. This shifting in band gap is maybe due to the metallic gray color of 1.5%Ag/SG sample [85] or the creation of lattice plasmons [86–88]. In addition, a particular feature to note in the UV–Vis DRS spectra in Fig. 6 is the rise of baseline of 1.5%Ag/SG’s spectrum with respect to that of SG, probably due the presence of silver plasmons.

Photo-activity of sol–gel nanocomposites

The photocatalyst amount in these tests was fixed at $1\ g\ L^{-1}$. Before testing SG, 1.5%Ag/SG and the reference AEROXIDE® TiO_2 P25, preliminary experiences of the adsorption for 1 h were carried out (Fig. 7). Apparently, the maximum equilibrium time was around 30 min; 1.5%Ag/SG and AEROXIDE® TiO_2 P25 exhibited low adsorption efficiency, while SG exhibited the highest one (5.3%), which may be explained by the clay content (37.3%).

Figure 8 shows the profile of phenol degradation and mineralization and the plot of $\ln(C/C_0)$ versus time with the investigated photocatalysts. It can be seen that SG showed 91% degradation and 81% mineralization. The photocatalytic test with this photocatalyst showed an activity ~ 1.5 -times better than that with AEROXIDE® TiO_2 P25. In fact, the plot of $\ln(C/C_0)$ versus time (Fig. 8b) gives respectively the k_{app} values of $0.019\ min^{-1}$ and $0.014\ min^{-1}$. The main explanation for the high SG activity is probably related to the structural modifications due to TiO_2 that act to promote the mobility of charge separation in the interstitial interior in order to promote the photo-oxidation process by avoiding recombination between the loaded TiO_2 and PT [89]. Doping of SG with 1.5% of silver enhanced the degradation efficiency from 91 to 95% with k_{app} value of $0.022\ min^{-1}$ and the mineralization from 81 to 83%. The increased activity of

Fig. 4 SEM photographs: **a** PT and **b** SG; **c** EDX mapping image of 1.5%Ag/SG



1.5%Ag/SG was caused by the photo-deposition of Ag, which increases the separation of generated electron–hole pairs, thus avoiding their recombination [74] (Scheme 1). In order to improve the photo-activity of 1.5%Ag/SG, we optimized the operating parameters (catalyst amount, pH, temperature, H₂O₂ concentration) in the next section.

Optimization of phenol photodegradation with 1.5%Ag/SG

The CCD model was adopted for investigating the optimization of the individual effects of the parameters screened

concerning the photodegradation of phenol by UV–1.5%Ag/SG system. Table 2 summarized the factors, ranges and levels of selected variables.

Based on the experimental design matrix proposed by CCD design (Table 3), the regression between the phenol degradation efficiency, coded variables, polynomials and corresponding interactions yields a second degree polynomial model (Eq. 3) which shows that the terms X_1 , X_3 , X_4 , X_1X_2 and X_1X_3 affect it positively, while X_2 , X_3X_4 , X_2X_4 , X_2X_3 , X_1X_4 , X_4^2 , X_3^2 , X_2^2 and X_1^2 affect it negatively. Catalyst amount (X_1) has a stronger effect between studied variables.

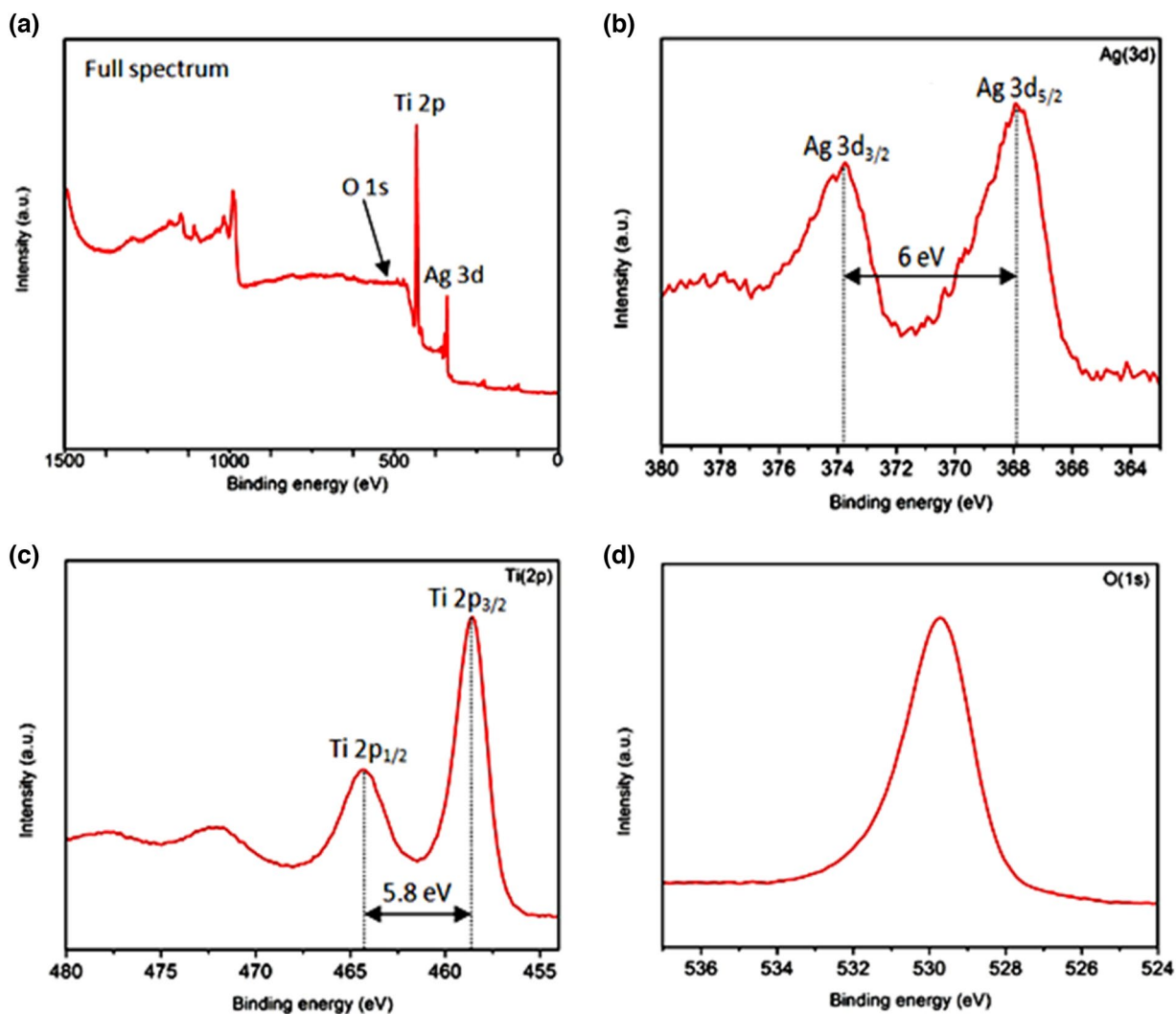


Fig. 5 XPS analysis of 1.5%Ag/SG: **a** Full spectrum, **b** Ag 3d XPS spectrum, **c** Ti 2p XPS spectrum, **d** O 1 s XPS spectrum

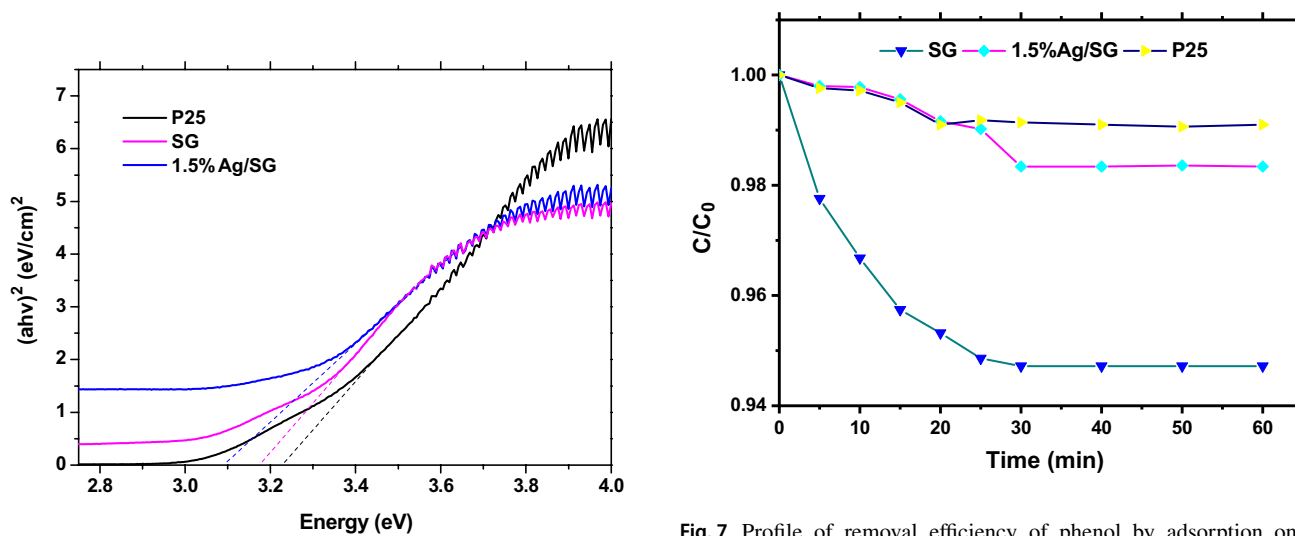


Fig. 6 UV-Vis DRS spectra of investigated photocatalysts

Fig. 7 Profile of removal efficiency of phenol by adsorption onto photocatalysts at [catalyst]=1 g mol⁻¹, room temperature, and not adjusted pH

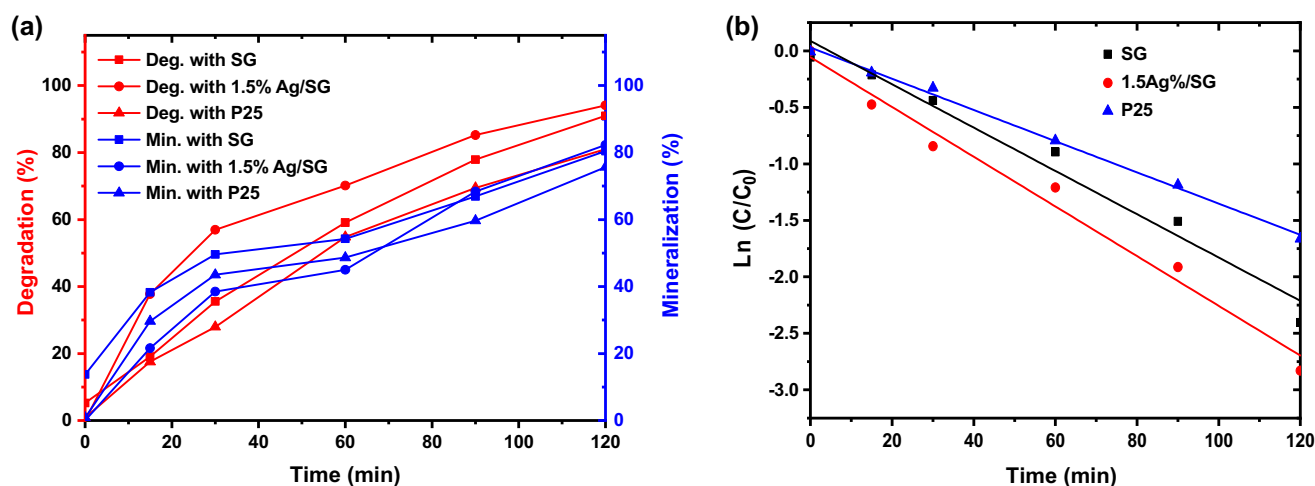
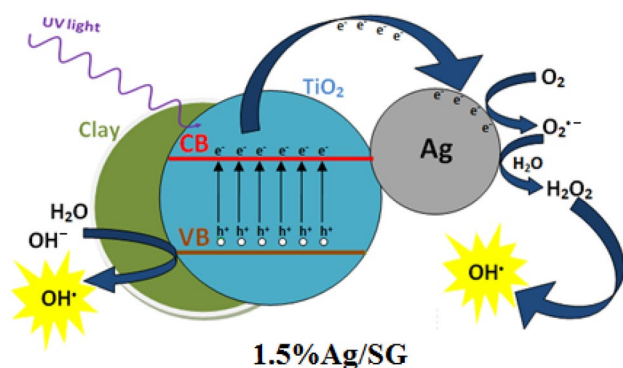


Fig. 8 Profile of degradation and mineralization of phenol versus time over photocatalysts at [catalyst] = 1 g mol⁻¹, room temperature, and not adjusted pH (a); Plot of $\ln(C/C_0)$ versus time (b)



Scheme 1. Diagram of the electron–hole pairs separation and corresponding redox reactions in the 1.5%Ag/SG nanoparticles

$$\begin{aligned}
 Y = & 78.73 + 14.56X_1 - 1.52X_2 + 7.01X_3 + 7.70X_4 + 2.57X_1X_2 \\
 & + 0.17X_1X_3 - 2.69X_1X_4 - 1.69X_2X_3 - 0.26X_2X_4 \\
 & - 0.96X_3X_4 - 1.75X_1^2 - 2.92X_2^2 - 4.57X_3^2 - 4.28X_4^2
 \end{aligned}
 \quad (3)$$

To confirm the quality of the fit for the determined coefficients, analysis of variance (ANOVA) was considered and the results are summarized in Table 4. According to such analysis, the low p value of (<0.0001) and the F -value of

73.31 are higher than critical F values for a 95% confidence level ($F_{9,10} = 3.02$ or $F_{9,7} = 3.8$), suggesting that the chosen model fits well [90–94].

Additionally, it can be seen that all terms, except X_1X_3 and X_2X_4 , such as linear (X_4 , X_3 , X_2 and X_1), interactions (X_3X_4 , X_2X_3 , X_1X_4 and X_1X_2) and quadratic (X_1^2 , X_2^2 , X_3^2 and X_4^2) are statistically significant (P value less than 0.05) [95]. The quality of the fit of the regression model can be confirmed by the coefficient of determination (R^2), which suggests that the variations in the degradation efficiency are considered by the model. Adjusted R^2 (R^2_{adj}) is also an indication of the quality of fit. It changes the R^2 considering the number of predictors in the model [26]. The fit statistics results are described in Table 5. The obtained R^2 and R^2_{adj} were high and very close, justifying that the model was well adjusted to the experimental data [27, 53].

The 3D and 2D response surface plots were used to show information on the effect of interactions on the % phenol degradation. The response surface plot based on interaction X_1X_2 (Fig. 9) has been selected in fact that its effect is positive and significant according to the model equation and ANOVA test, respectively. Thus, the optimum conditions for phenol degradation under the postulated model are described in Table 6.

Table 2 Coded and real values of the parameters for CCD design

Independent variable	Factors X_i	Range and level			Star point	
		Low (-1)	Central (0)	High (1)	-2	2
Catalyst amount (g/L)	X_1	1	1.5	2	0.5	2.5
pH	X_2	4	6	8	2	10
Temperature (°C)	X_3	30	40	50	20	60
H ₂ O ₂ concentration (mmol L ⁻¹)	X_4	6	8	10	4	12

Table 3 Design matrix with the experimental and predicted responses of phenol degradation (%)

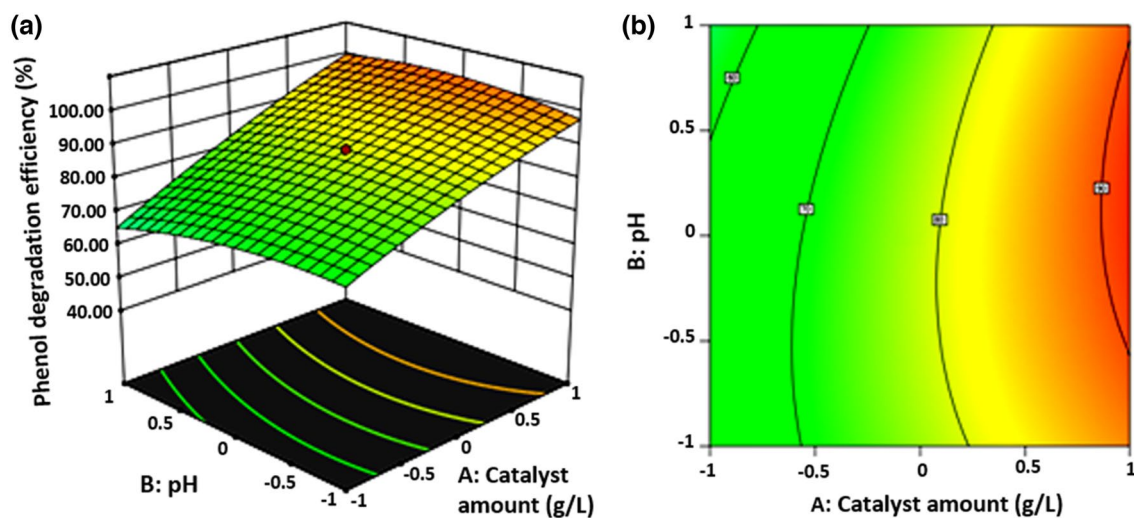
Run	Coded variables				Phenol degradation efficiency (%)		
	X_1	X_2	X_3	X_4	Experimental	Predicted	Residual
1	-1	1	-1	1	51.90	52.5	-0.60
2	1	1	1	-1	84.10	82.49	1.61
3	0	0	0	-2	45.30	46.19	-0.89
4	-1	-1	1	-1	53.90	53.58	0.32
5	0	0	0	0	78.80	78.73	0.07
6	0	0	0	0	78.60	78.73	0.01
7	0	2	0	0	63.80	63.99	-0.19
8	-1	-1	-1	-1	34.90	34.61	0.29
9	0	0	0	0	78.80	78.73	0.07
10	1	-1	1	1	93.30	91.91	1.39
11	0	0	0	2	75.60	77.00	-1.40
12	-1	1	1	1	61.40	60.88	0.52
13	1	-1	1	-1	84.50	83.27	1.23
14	2	0	0	0	99.20	100.87	-1.67
15	0	0	2	0	71.59	74.48	-2.89
16	1	-1	-1	-1	64.77	63.63	1.14
17	1	1	-1	-1	68.20	69.63	-1.43
18	0	0	-2	0	47.06	46.46	0.60
19	-1	1	-1	-1	30.60	30.33	0.27
20	1	-1	-1	1	76.10	76.09	0.01
21	-1	1	1	-1	43.16	42.53	0.63
22	1	1	-1	1	82.40	81.06	1.34
23	-1	-1	1	1	75.03	72.97	2.06
24	0	-2	0	0	67.98	70.08	-2.10
25	-2	0	0	0	42.01	42.63	-0.62
26	-1	-1	-1	1	57.87	57.82	0.05
27	1	1	1	1	90.44	90.1	0.34

Table 4 Analysis of variance (ANOVA) for CCD design

Source of variation	Sum of squares	Df	Mean of squares	F-value	p value
Model	8679.68	14	619.98	207.06	<0.0001
X_1	5087.56	1	5087.56	1699.13	<0.0001
X_2	55.6	1	55.6	18.57	0.001
X_3	1178.1	1	1178.1	393.46	<0.0001
X_4	1424.65	1	1424.65	475.8	<0.0001
X_1X_2	105.63	1	105.63	35.28	<0.0001
X_1X_3	0.4389	1	0.4389	0.1466	0.7085
X_1X_4	115.4	1	115.4	38.54	<0.0001
X_2X_3	45.87	1	45.87	15.32	0.0021
X_2X_4	1.08	1	1.08	0.3595	0.5599
X_3X_4	14.61	1	14.61	4.88	0.0474
X_1^2	65.01	1	65.01	21.71	0.0006
X_2^2	182.46	1	182.46	60.94	<0.0001
X_3^2	444.71	1	444.71	148.52	<0.0001
X_4^2	391.61	1	391.61	130.79	<0.0001
Residual	35.93	12	2.99		
Total	8715.61	26			

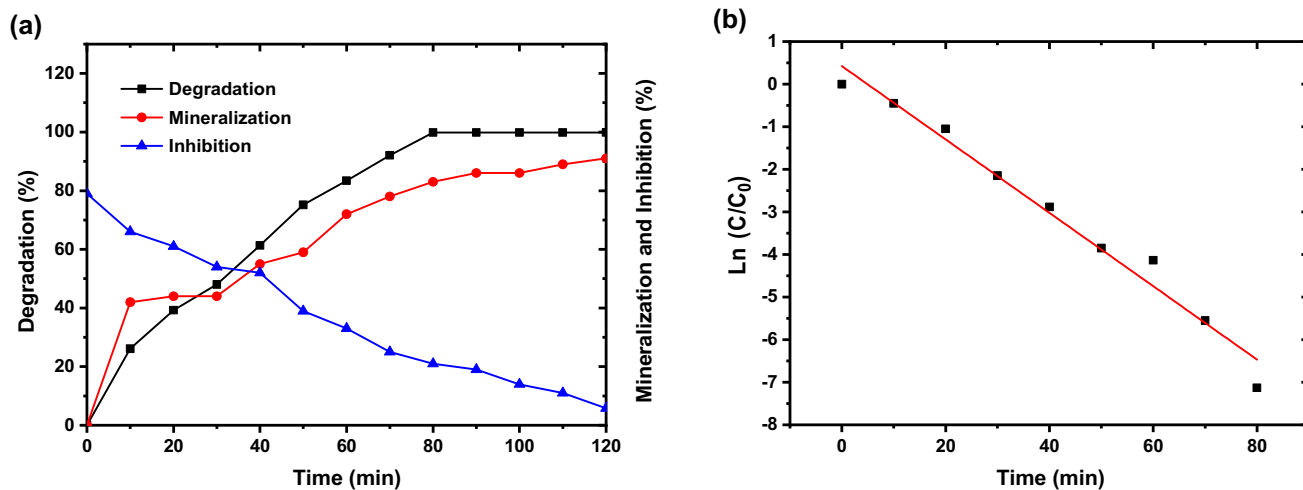
Table 5 Fit statistics results

Std. dev	Mean	C.V. %	R^2	Adjusted R^2	Predicted R^2	Adeq. precision
1.73	66.72	2.59	0.9959	0.9911	0.9763	54.69

**Fig. 9** The 3D (a) and 2D (b) response surface plots for the interactive effect of pH and catalyst amount**Table 6** Optimized parameters obtained from response surface analysis

Catalyst amount (g L ⁻¹)	pH	Temperature	H ₂ O ₂ concentration (mmol L ⁻¹)	Degradation efficiency (%)	
				Predicted	Experimental
2	5	40	8	99.84	100

Under these optimum conditions, an experimental experience was carried out (Fig. 10). It can be seen that the degradation efficiency was 100% with mineralization of 91% for 120 min of reaction (Fig. 10a). Additionally, the treated solution was not toxic based on the bioluminescence inhibition test of *Vibrio Fischeri* bacteria, it showed 5.8% of inhibition which is less than the normalized one of 10%. The analysis of the curve $\ln(C_0/C) = f(t)$ under optimized conditions

**Fig. 10** At optimized parameters ([catalyst]=2 g mol⁻¹, pH=5, T=40 °C, and [H₂O₂]=8 mmol L⁻¹): profile of degradation, mineralization and toxicity (a) and plot of $\ln(C/C_0)$ versus time with 1.5%Ag/SG (b)

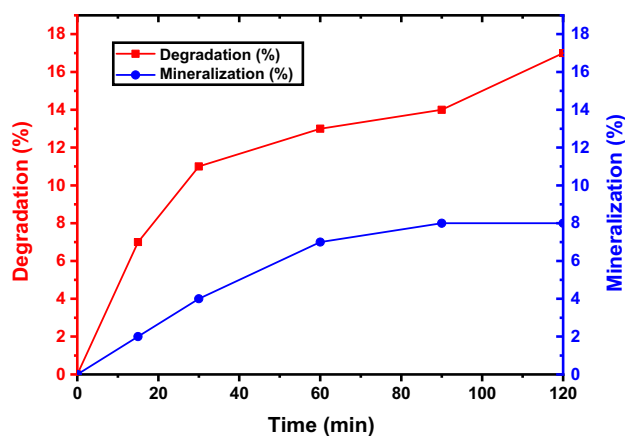


Fig. 11 Profile of degradation and mineralization with UV/H₂O₂ system, at pH=5, T=40 °C, and [H₂O₂]=8 mmol L⁻¹

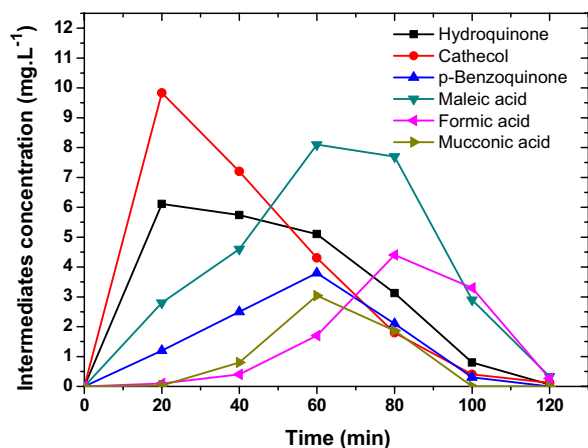


Fig. 12 Profile of intermediates concentration at optimized parameters

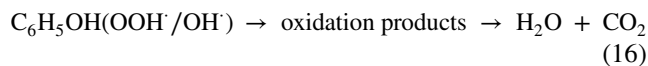
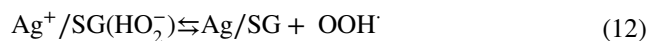
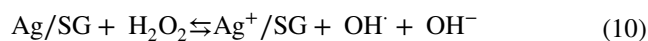
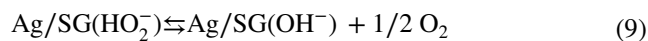
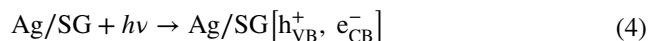
(Fig. 10b) showed K_{app} of 0.08 min^{-1} , which is ~4-times faster than that found before optimization (0.022 min^{-1}).

Figure 11 shows the evaluation of degradation and mineralization at optimal conditions without photocatalyst during 120 min of irradiation. It can be seen that the photolysis of H₂O₂ molecules was not negligible, but has not mainly affected the above optimized degradation, with respect to the obtained percentages of degradation (17%) and mineralization (8%). These results further suggest that 1.5%Ag/SG is very active in the UV degradation of phenol.

Figure 12 presents the profile of intermediates concentration (hydroquinone, *p*-benzoquinone, catechol, maleic acid, formic acid, muconic acid) at optimum conditions with 1.5%Ag/SG during 120 min of irradiation. The concentrations of the intermediates increased with irradiation time until reaching an optimum, after which they started to decrease. This evolution can be attributed to the continuous

radical degradation of phenol until mineralization to H₂O and CO₂. The aromatic intermediates resulting from the degradation of phenol (catechol, hydroquinone, *p*-benzoquinone) can be converted into carboxylic acids like oxalic, formic, maleic and acetic [96, 97]. The final concentration of intermediates was very low, thus confirming the non-toxicity and mineralization of the treated solutions. Scheme 2 illustrated the proposed pathway of studied phenol degradation.

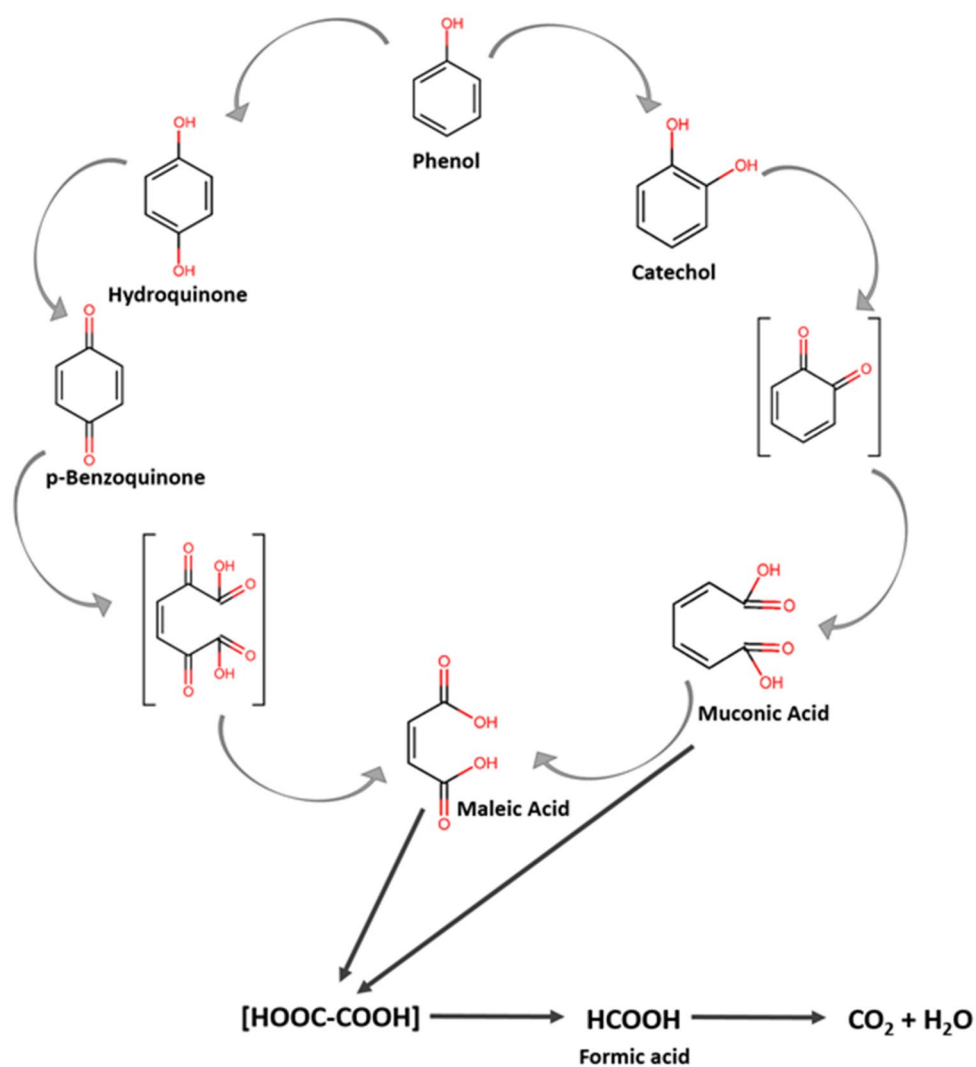
The investigated phenol degradation at optimized conditions might be described in the presence of silver-TiO₂ particles and H₂O₂ agent for which the following mechanism may thus be suggested:



Conclusion

The heterogeneous photocatalysis process was investigated in the degradation of phenol under UV irradiation using sol–gel nanocomposites as photocatalysts. Natural pyrophyllite and titanium (IV) *t*-butoxide were used as support and precursor, respectively. The TiO₂-clay nanocomposite (SG), the silver-photodeposited nanocomposite 1.5%Ag/SG and

Scheme 2. Proposed pathways for photodegradation of phenol over 1.5%Ag/SG



the reference AEROXIDE® TiO₂ P25 were characterized by XRD, XPS, UV–Vis DRS and BET surface area. The degradation and TOC mineralization with SG at catalyst amount of 1 g L⁻¹ and phenol concentration of 50 mg L⁻¹ was higher than that found with AEROXIDE® TiO₂ P25. The photocatalytic performance of the studied reaction was enhanced using 1.5%Ag/SG; in fact, the degradation and TOC mineralization efficiencies were increased from 91 and 81% to 94.2 and 82.3%, respectively. 4-level composite central design (CCD) in response surface methodology (RSM), was used to optimize the degradation of phenol with 1.5%Ag/SG. Various process parameters were optimized by using CCD, viz., catalyst amount (X_1 : 0.5–2.5 g L⁻¹), solution pH (X_2 : 2–10), temperature (X_3 : 20–60 °C), and Hydrogen peroxide concentration (X_4 : 4–12 mmol L⁻¹). According to CCD design, the second-degree polynomial model correlates the parameters to % degradation of phenol. The significance of this model

and regression coefficients was examined by the analysis of variance (ANOVA). This analysis indicated that the selected model was well fitted and correlated to experimental data (p value < 0.001, F -value = 73.31, R^2 = 0.9959). The optimum parameters were photocatalyst amount of 2 g L⁻¹, solution pH of 5, and the temperature of 40 °C and hydrogen peroxide concentration of 8 mmol L⁻¹. The highest % degradation efficiency of 100%, with a constant rate ~ 4-times greater than that found before optimization, was observed based on the interaction X_1X_2 . Furthermore, non-toxicity and good mineralization (91%) were also observed under optimized conditions.

Acknowledgements The authors gratefully acknowledge the collaborations of Innovation Center, Sidi Mohamed Ben Abdellah University of Fez, Morocco.

Funding No funding was received for this study.

Declarations

Conflict of interest All authors certify that they have no conflicts of interests associated with this publication.

References

- A. Fegousse, A. El Gaidoumi, Y. Miyah, R. El Mountassir, A. Lahrichi, *J. Chem.* **2019**, 1–11 (2019)
- A. Battas, A. El Gaidoumi, A. Ksakas, A. Kherbeche, *Sci. World J.* **2019**, 1–10 (2019)
- A. Dra, A. El Gaidoumi, K. Tanji, A. Chaouni Benabdallah, A. Taleb, A. Kherbeche, *Sci. World J.* **2019**, 21 (2019)
- A. Loqman, B. El Bali, A. El Gaidoumi, A. Boularbah, A. Kherbeche, *J. Lützenkirchen, Silicon* **2021**, 1 (2021)
- O. Mertah, K. El Hajjaji, A. El Gaidoumi, A. Lachehab, H. Hassoune, A. Kherbeche, *Opt. Quantum Electron.* **52**, 1 (2020)
- M. Zouheir, O. Assila, K. Tanji, A. El Gaidoumi, J. Araña, J.M. Doña Rodríguez, J.-H. Smätt, T.-P. Huynh, A. Kherbeche, *Nano Futur.* **5**, 025004 (2021)
- A. Dra, K. Tanji, A. Arrahli, E.M. Iboustaten, A. El Gaidoumi, A. Kherchafi, A. Chaouni Benabdallah, A. Kherbeche, *Sci. World J.* **2020**, 8 (2020)
- S. Sohrabi, F. Akhlaghian, *J. Iran. Chem. Soc.* **13**, 1785 (2016)
- D. Kale, P. Thakur, *J. Porous Mater.* **22**, 797 (2015)
- S. Yapar, P. Klahre, E. K.-T. J. Eng undefined 2004, *J. Tubitak. Gov. Tr* **28**, 41 (2004)
- M. Akçay, *J. Colloid Interface Sci.* **280**, 299 (2004)
- Y. Fahoul, M. Zouheir, K. Tanji, A. Kherbeche, *J. Alloys Compd.* **889**, 161708 (2021)
- M. Zouheir, O. Assila, K. Tanji, A. El Gaidoumi, J. Araña, J.M.D. Rodríguez, J.-H. Smätt, T.-P. Huynh, A. Kherbeche, *Nano Futur.* **5**, 025004 (2021)
- A. Thiam, K. Tanji, O. Assila, M. Zouheir, R. Haounati, A. Arrahli, A. Abeid, S. Lairini, R. Bouslamti, F. Zerouq, A. Kherbeche, *J. Chem.* **2020**, 14 (2020)
- K. Tanji, M. Zouheir, Y. Naciri, H. Ahmoum, A. Hsini, O. Mertah, *J. Iran. Chem. Soc.* **19**, 2779 (2022)
- N. Assi, M.S. Tehrani, P.A. Azar, S.W. Husain, *J. Iran. Chem. Soc.* **14**, 221 (2017)
- Y. Fahoul, K. Tanji, M. Zouheir, I. El, Y. Naciri, A. Hsini, L. Nahali, A. Kherbeche, *J. Mol. Struct.* **1253**, 132298 (2022)
- B.H. Hameed, A.A. Rahman, *J. Hazard. Mater.* **160**, 576 (2008)
- S.Z. Wu, N. Li, W. De Zhang, *J. Porous Mater.* **21**, 157 (2014)
- M.A. Fox, M.T. Dulay, *Chem. Rev.* **93**, 341 (2002)
- B. Aicha, S. Mohamed, M.B. Jocelyne, L. Benedicte, B. Jean-Luc, B. Abdelkader, *J. Porous Mater.* **25**, 801 (2018)
- H. Xu, S. Sun, S. Jiang, H. Wang, R. Zhang, Q. Liu, *J. Sol-Gel Sci. Technol.* **87**, 676 (2018)
- X. Zhao, Y. Meng, X. Lu, X. Li, *J. Sol-Gel Sci. Technol.* **66**, 22 (2013)
- J. Liu, G. Zhang, *Phys. Chem. Chem. Phys.* **16**, 8178 (2014)
- S. Perathoner, G. Centi, *Pillared Clays and Related Catalysts* (Springer, New York, 2010), p.167
- L. Chmielarz, B. Gil, P. Kuśtrowski, Z. Piwowarska, B. Dudek, M. Michalik, *J. Solid State Chem.* **182**, 1094 (2009)
- C. Belver, P. Aranda, M.A. Martín-Luengo, E. Ruiz-Hitzky, *Microporous Mesoporous Mater.* **147**, 157 (2012)
- M.M. Khan, S.A. Ansari, M.O. Ansari, B.K. Min, J. Lee, M.H. Cho, *J. Phys. Chem. C* **118**, 9477 (2014)
- R. Saravanan, V.K. Gupta, V. Narayanan, A. Stephen, *J. Taiwan Inst. Chem. Eng.* **45**, 1910 (2014)
- S. Oros-Ruiz, R. Zanella, R. López, A. Hernández-Gordillo, R. Gómez, *J. Hazard. Mater.* **263**, 2 (2013)
- R. Saravanan, V.K. Gupta, T. Prakash, V. Narayanan, A. Stephen, *J. Mol. Liq.* **178**, 88 (2013)
- M.R. Espino-Estévez, C. Fernández-Rodríguez, O.M. González-Díaz, J. Araña, J.P. Espinós, J.A. Ortega-Méndez, J.M. Doña-Rodríguez, *Chem. Eng. J.* **298**, 82 (2016)
- J.J. Murcia, M.C. Hidalgo, J.A. Navío, J. Araña, J.M. Doña-Rodríguez, *Appl. Catal. B Environ.* **179**, 305 (2015)
- J.J. Murcia, M.C. Hidalgo, J.A. Navío, J. Araña, J.M. Doña-Rodríguez, *Appl. Catal. B Environ.* **150–151**, 107 (2014)
- E. Pulido Melián, O. González Díaz, J.M. Doña Rodríguez, G. Colón, J.A. Navío, M. Macías, J. Pérez Peña, *Appl. Catal. B Environ.* **127**, 112 (2012)
- M.J. Hernández Rodríguez, E. Pulido Melián, D. García Santiago, O. González Díaz, J.A. Navío, J.M. Doña Rodríguez, *Appl. Catal. B Environ.* **205**, 148 (2017)
- E.P. Melián, C.R. López, D.E. Santiago, R. Quesada-Cabrera, J.A.O. Méndez, J.M.D. Rodríguez, O.G. Díaz, *Appl. Catal. A Gen.* **518**, 189 (2016)
- C.R. López, E.P. Melián, J.A. Ortega Méndez, D.E. Santiago, J.M. Doña Rodríguez, O. González Díaz, *J. Photochem. Photobiol. A Chem.* **312**, 45 (2015)
- J.A. Ortega Méndez, C.R. López, E. Pulido Melián, O. González Díaz, J.M. Doña Rodríguez, D. Fernández Hevia, M. Macías, *Appl. Catal. B Environ.* **147**, 439 (2014)
- C. Suwanchawalit, S. Wongnawa, P. Sriprang, P. Meanha, *Ceram. Int.* **38**, 5201 (2012)
- H. Tran, J. Scott, K. Chiang, R. Amal, *J. Photochem. Photobiol. A Chem.* **183**, 41 (2006)
- A. Sclafani, M.N. Mozzanega, P. Pichat, *J. Photochem. Photobiol. A Chem.* **59**, 181 (1991)
- M.M. Kondo, W.F. Jardim, *Water Res.* **25**, 823 (1991)
- Y. Zhang, T. Wang, M. Zhou, Y. Wang, Z. Zhang, *Ceram. Int.* **43**, 3118 (2017)
- X. Wang, T. Li, R. Yu, H. Yu, J. Yu, *J. Mater. Chem. A* **4**, 8682 (2016)
- N. Roy, K.T. Leung, D. Pradhan, *J. Phys. Chem. C* **119**, 19117 (2015)
- L. Li, X. Zhang, W. Zhang, L. Wang, X. Chen, Y. Gao, *Colloids Surf A Physicochem. Eng. Asp.* **457**, 134 (2014)
- S. Mohammadnejad, J.L. Provis, J.S.J. Van Deventer, *Hydrometallurgy* **146**, 154 (2014)
- J. Zhang, J. Yan, J. Sheng, *Micron* **71**, 1 (2015)
- S. Saxena, M. Prasad, S.S. Amritphale, N. Chandra, *Sep. Purif. Technol.* **24**, 263 (2001)
- R. Keren, D.L. Sparks, *Soil Sci. Soc. Am. J.* **58**, 1095 (1994)
- R.G. Ford, D.L. Sparks, *Environ. Sci. Technol.* **34**, 2479 (2000)
- M. Prasad, S. Saxena, S.S. Amritphale, N. Chandra, *Ind. Eng. Chem. Res.* **39**, 3034 (2000)
- A. El Gaidoumi, A. Loqman, A.C. Benabdallah, B. El Bali, A. Kherbeche, *Waste Biomass Valoriz.* **10**, 1043 (2019)
- A. El Gaidoumi, A. Chaouni Benabdallah, B. El Bali, A. Kherbeche, *Arab. J. Sci. Eng.* **43**, 191 (2017)
- A. El Gaidoumi, J.M. Doña-Rodríguez, E. Pulido Melián, O.M. González-Díaz, B. El Bali, J.A. Navío, A. Kherbeche, *Res. Chem. Intermed.* **45**, 333 (2019)
- A. El Gaidoumi, A. Kherbeche, E. Gaidoumi, A. El Gaidoumi, A.C. Benabdallah, A. Lahrichi, A. Kherbeche, *J. Mater. Environ. Sci.* **6**, 2247 (2015)
- A. El Gaidoumi, J.M. Doña-Rodríguez, E. Pulido Melián, O.M. González-Díaz, J.A. Navío, B. El Bali, A. Kherbeche, *Arab. J. Sci. Eng.* **44**, 6313 (2019)
- A. El Gaidoumi, J.M. Doña Rodríguez, E. Pulido Melián, O.M. González-Díaz, J.A. Navío Santos, B. El Bali, A. Kherbeche, *Surf. Interfaces* **14**, 19 (2019)

60. A. El Gaidoumi, A. Loqman, M. Zouheir, K. Tanji, O. Mertah, A. Dra, B. El Bali, A. Kherbeche, A. El Gaidoumi, A. Loqman, M. Zouheir, K. Tanji, O. Mertah, A. Dra, B. El Bali, A. Kherbeche, *Res. Chem. Intermed.* **47**, 1 (2021)
61. A. El Gaidoumi, A. Arrahli, A. Loqman, F. Baragh, B. El Bali, A. Kherbeche, *Silicon* **2021**, 1 (2021)
62. Z. Meçabih, S. Kacimi, B. Bouchikhi, *Rev. Des Sci. l'Eau* **19**, 23 (2006)
63. A.K.T. Mohammad, A.S. Abdulhameed, A.H. Jawad, *Int. J. Biol. Macromol.* **129**, 98 (2019)
64. A. Bentayeb, M. Amouric, J. Olives, A. Dekayir, A. Nadiri, *Appl. Clay Sci.* **22**, 211 (2003)
65. G. Li, J. Zeng, J. Luo, M. Liu, T. Jiang, G. Qiu, *Appl. Clay Sci.* **99**, 282 (2014)
66. M. Erdemoğlu, S. Erdemoğlu, F. Sayilkan, M. Akarsu, Ş Şener, H. Sayilkan, *Appl. Clay Sci.* **27**, 41 (2004)
67. N. Hamzah, N.M. Nordin, A.H.A. Nadzri, Y.A. Nik, M.B. Kassim, M.A. Yarmo, *Appl. Catal. A Gen.* **419–420**, 133 (2012)
68. X. Zhao, J. Li, Y. Zhang, H. Dong, J. Qu, T. Qi, *Powder Technol.* **271**, 262 (2015)
69. A. Gil, S.A. Korili, M.A. Vicente, *Catal. Rev.* **50**, 153 (2008). <https://doi.org/10.1080/01614940802019383>
70. L. Gao, W. Gan, S. Xiao, X. Zhan, J. Li, *Ceram. Int.* **42**, 2170 (2016)
71. X. Zhao, J. Li, Y. Liu, Y. Zhang, J. Qu, T. Qi, *Dyes Pigments* **108**, 84 (2014)
72. L. Gao, X. Zhan, Y. Lu, J. Li, Q. Sun, *Mater. Lett.* **142**, 217 (2015)
73. J. Li, Suyoulema, W. Wang, Sarina, *Solid State Sci.* **11**, 2037 (2009).
74. T. Wang, J. Wei, H. Shi, M. Zhou, Y. Zhang, Q. Chen, Z. Zhang, *Phys. E Low-Dimens. Syst. Nanostruct.* **86**, 103 (2017)
75. C. Belver, J. Bedia, J.J. Rodriguez, *Appl. Catal. B Environ.* **176–177**, 278 (2015)
76. K.S.W. Sing, R.T. Williams, *Part. Part. Syst. Charact.* **21**, 71 (2004)
77. J. Rouquerol, F. Rouquerol, P. Llewellyn, G. Maurin, K.S.W. Sing, *Adsorption by Powders and Porous Solids: Principles, Methodology, and Applications*, 2nd edn. (Elsevier Inc., 2013)
78. H. Bel Hadjitaief, M.E. Galvez, M. Ben Zina, P. Da Costa, *Arab. J. Chem.* **12**, 1454 (2014)
79. B. Krishnan, S. Mahalingam, *Adv. Powder Technol.* **28**, 2265 (2017)
80. L. Zhang, D. Shi, B. Liu, G. Zhang, Q. Wang, J. Zhang, *CrystEng-Comm* **18**, 6444 (2016)
81. D.B. Nguyen, T.D.C. Nguyen, T.P. Dao, H.T. Tran, V.N. Nguyen, D.H. Ahn, *J. Ind. Eng. Chem.* **18**, 1764 (2012)
82. C. Wang, E. Yifeng, L. Fan, S. Yang, Y. Li, *J. Mater. Chem.* **19**, 3841 (2009)
83. S.A. Ansari, M.M. Khan, M.O. Ansari, M.H. Cho, *Sol. Energy Mater. Sol. Cells* **141**, 162 (2015)
84. B.K. Sarma, A.R. Pal, H. Bailung, J. Chutia, *J. Phys. D: Appl. Phys.* **45**, 275401 (2012)
85. J.J. Murcia, M.C. Hidalgo, J.A. Navío, V. Vaiano, P. Ciambelli, D. Sannino, *Catal. Today* **196**, 101 (2012)
86. E. Kowalska, O.O.P. Mahaney, R. Abe, B. Ohtani, *Phys. Chem. Chem. Phys.* **12**, 2344 (2010)
87. L.S. Daniel, H. Nagai, N. Yoshida, M. Sato, *Catalysts* **3**, 625–645 (2013)
88. N. Zhang, S. Liu, X. Fu, Y.J. Xu, *J. Phys. Chem. C* **115**, 9136 (2011)
89. C. Belver, J. Bedia, M.A. Álvarez-Montero, J.J. Rodriguez, *Catal. Today* **266**, 36 (2016)
90. H. Li, Y. Li, L. Xiang, Q. Huang, J. Qiu, H. Zhang, M.V. Sivaiah, F. Baron, J. Barrault, S. Petit, S. Valange, *J. Hazard. Mater.* **287**, 32 (2015)
91. O.B. Ayodele, J.K. Lim, B.H. Hameed, *Chem. Eng. J.* **197**, 181 (2012)
92. L.C. Almeida, S. Garcia-Segura, N. Bocchi, E. Brillias, *Appl. Catal. B Environ.* **103**, 21 (2011)
93. J. Herney-Ramirez, M. Lampinen, M.A. Vicente, C.A. Costa, L.M. Madeira, *Ind. Eng. Chem. Res.* **47**, 284 (2008)
94. F. Torrades, J. García-Montaño, *Dyes Pigments* **100**, 184 (2014)
95. A.M. Scheidegger, G.M. Lamble, D.L. Sparks, *Environ. Sci. Technol.* **30**, 548 (1996)
96. H.R. Devlin, I.J. Harris, *Ind. Eng. Chem. Fundam.* **23**, 387 (2002)
97. D. Duprez, F. Delanoë, J. Barbier, P. Isnard, G. Blanchard, *Catal. Today* **29**, 317 (1996)

Springer Nature or its licensor holds exclusive rights to this article under a publishing agreement with the author(s) or other rightsholder(s); author self-archiving of the accepted manuscript version of this article is solely governed by the terms of such publishing agreement and applicable law.